

Article

Formation of the Lened W-(Be) Skarn Deposit by Neutralization of a Magmatic Fluid—Evidence from H₃BO₃-Rich Fluids

Hélène Legros ^{1,*}, Vanessa Elongo ¹, Oscar Laurent ^{2,3}, Erin Adlakha ⁴, Cyril Chelle-Michou ², Hendrik Falck ⁵ and Pilar Lecumberri-Sanchez ¹

¹ Department of Earth and Atmospheric Sciences, University of Alberta, Edmonton, AB T6G 2E3, Canada; elongo@ualberta.ca (V.E.); lecumber@ualberta.ca (P.L.-S.)

² Institute of Geochemistry and Petrology, ETH Zurich, 8092 Zurich, Switzerland; oscar.laurent@get.omp.eu (O.L.); cyril.chelle-michou@erdw.ethz.ch (C.C.-M.)

³ CNRS, Géosciences Environnement Toulouse, Observatoire Midi-Pyrénées, 31400 Toulouse, France

⁴ Department of Geology, Saint Mary's University, 923 Robie St., Halifax, NS B3H 3C3, Canada; erin.adlakha@smu.ca

⁵ Northwest Territories Geological Survey, 5310 44 St., Yellowknife, NWT X1A 1K3, Canada; hendrik_falck@gov.nt.ca

* Correspondence: hlegros@ualberta.ca



Citation: Legros, H.; Elongo, V.; Laurent, O.; Adlakha, E.; Chelle-Michou, C.; Falck, H.; Lecumberri-Sanchez, P. Formation of the Lened W-(Be) Skarn Deposit by Neutralization of a Magmatic Fluid—Evidence from H₃BO₃-Rich Fluids. *Geosciences* **2022**, *12*, 236. <https://doi.org/10.3390/geosciences12060236>

Academic Editors: Paul A. Mueller and Jesus Martinez-Frias

Received: 1 April 2022

Accepted: 30 May 2022

Published: 2 June 2022

Publisher's Note: MDPI stays neutral with regard to jurisdictional claims in published maps and institutional affiliations.



Copyright: © 2022 by the authors. Licensee MDPI, Basel, Switzerland. This article is an open access article distributed under the terms and conditions of the Creative Commons Attribution (CC BY) license (<https://creativecommons.org/licenses/by/4.0/>).

Abstract: Magmatic-hydrothermal systems, especially those causing the formation of tungsten deposits, may be enriched in boron, as is suggested by the presence of hydrothermal tourmaline. This study examines the boron and metal (including tungsten) concentrations of quartz-hosted fluid inclusions in the Lened W-(Be) deposit of the Canadian Cordillera and resolves (i) the analytical challenges involved during fluid salinity calculations of B-rich fluids and (ii) the relationship between fluid chemical composition and ore-forming processes involved at Lened. The aqueous fluid inclusions from this study have high CO₂ and boron contents, indicated by the presence of a carbonic phase and sassolite crystals (H₃BO₃) in fluid inclusions. The boron content of the aqueous liquid phase (0.5 wt. %) was determined using microthermometric and Raman spectroscopic analyses. Boron was judged the most appropriate internal standard for quantifying the LA-ICP-MS data from these inclusions after calculation of salinity in the H₂O-NaCl-H₃BO₃ system (3.5 to 5 wt. % NaCl_{eq}). Trace element data of the fluids show relatively high concentrations of Li (40 to 474 ppm), Al (56 to 1003 ppm), As (36 to 490 ppm) and Cs (68 to 296 ppm); and lower concentrations of Rb (3.6 to 77 ppm), Sr (0.4 to 23 ppm), Sb (1 to 32 ppm), Ba (0.6 to 163 ppm), Mg (6.9 to 7.6 ppm) and other metals, such as Be (2.4 to 10.2 ppm), W (2.4 to 27 ppm) and Cu (5.1 to 73 ppm). The high Cs and Li concentrations suggest a magmatic origin of the metals, while the moderate concentrations in Sr and Ba are indicative of fluid–rock interaction with the surrounding limestone. The presence of sassolite suggests that these fluids were highly acidic. The neutralization of this fluid through interaction with the surrounding limestone is the most probable trigger for scheelite precipitation. The presence of such high boron content in the magmatic fluid at Lened indicates the potential role in the enrichment of the source melt before fluid exsolution.

Keywords: fluid inclusion; sassolite; Lened; boron; emerald; scheelite

1. Introduction

High boron concentrations are typical of evolved magmas and their associated magmatic-hydrothermal ore deposits [1–3]. Specifically, tungsten and beryllium-rich magmatic-hydrothermal systems are associated with highly differentiated peraluminous granites and are responsible for the precipitation of emerald and tungsten minerals (such as scheelite) in veins and skarns [4–6]. High boron in these systems is indicated by extensive tourmalinization associated with greisen and hydrothermal veins [5,7–10]. In fact, tourmaline has been widely used as a tracer of the magmatic-hydrothermal processes because of its systematic

presence [3,11–16]. Additionally, fluid inclusions that contain up to 1 wt. % boron have been reported in magmatic-hydrothermal tungsten deposits [17,18], making boron a major component of the mineralizing fluid.

The physical and chemical properties of silicate melts are strongly affected by boron concentrations [19–21]. In particular, high boron increases H₂O solubility in granitic melts, allowing the residual melt to crystallize down to temperatures of 600 °C [22]. For example, 1 wt. % B in a haplogranitic melt at 1–2 kbar would increase its H₂O concentration by ca. 3–4 wt. % and decrease its solidus by ca. 100 °C [23]. The protracted magmatic differentiation processes enhance enrichment of incompatible elements, such as tungsten or beryllium, in the residual melts and fluids.

The Lened W-(Be) skarn, located in the Canadian Cordillera, shows evidence of tourmaline, beryl-emerald and scheelite in the same quartz veins, and therefore offers the possibility to investigate the ore processes that involve boron, beryllium and tungsten. Moreover, the Lened W-(Be) deposit fluid inclusions hosted in quartz exhibit sassolite crystals (H₃BO₃), which is a rare occurrence, indicative of boron saturation of the fluid, offering the possibility to document whether the high concentration of boron has an impact on the metal budget of the fluid. The current literature on trace element concentrations of fluid inclusions in W- and Be-rich systems includes only a single article on the trace elements of fluids that produce W skarns [24] and another article on gem beryl deposits [25]. Robust LA-ICP-MS analyses of sassolite-bearing fluid inclusions from Lened are an excellent opportunity to document the trace element concentrations of boron-rich fluids. This article aims at documenting these uncommon fluid inclusions related to boron-rich ore fluids, but also discusses the challenges of salinity calculations in a system including H₃BO₃ as one of the main components, and evaluates the uncertainties associated with using salinity to calculate trace element abundances.

2. Geological Setting of the Lened W-(Be) Deposit

The Lened deposit is located within the Tungsten Belt, near the border between the Yukon and the Northwest Territories (Canada). It includes gem-quality emerald-bearing quartz veins [26,27] and W skarn prospects [28,29] (Figure 1A). These veins cross-cut the sedimentary country rocks and are spatially associated with the Lened pluton [30], which is extensively intruded by genetically associated dikes and faults [26]. The W resources are estimated at 0.9 Mt grading 1.0% WO₃; but the deposit is considered a sub-economic resource because of its isolated location [31]. The Lened pluton, which belongs to the Selwyn Plutonic Suite, is a multiphase, two-mica quartz monzonite/granite [26] of mid-Cretaceous age (zircon U-Pb age of 97.6 ± 0.8 Ma [2 σ]; biotite Ar-Ar age of 94.8 ± 0.6 Ma [2 σ]; [30]). The pluton is approximately 7 km long and 4 km wide [32]. The granite outcrops in the vicinity of the Lened skarn and emerald vein prospects.

The stratigraphic succession in the Lened area includes four major sedimentary units from late Proterozoic to Cretaceous age (Figure 1B). The oldest unit is the late Proterozoic to Lower Cambrian Vampire Formation (Fm) consisting of phyllitic shale, siltstone and very fine to fine-grained sandstone [32,33]. The Vampire Fm is overlain by the Cambrian-Ordovician Rabbitkettle Fm composed of dark grey, thin to medium-bedded limestone with argillaceous to silty layers, and whitish grey dolomitic limestone to dark grey calcareous siltstones [26,32,33]. Southwest of Lened, the lower part of the Rabbitkettle Fm transitions to the sandy dolostone and limestone facies of the Haywire Fm that rest unconformably on the Vampire Fm [33]. Black shale, chert and sandstone conglomerate belonging to the Ordovician-Silurian Duo Lake Fm (Road River Group) and the Devonian-Mississippian Portrait Lake Fm (Earn Group) have not been differentiated and are collectively referred to as black mudstone in Figure 1B, covering most of the Rabbitkettle Fm along a thrust fault contact [26,32,33]. The whole sedimentary sequence is structurally deformed by the regional Jurassic–Cretaceous contraction that caused northwest-trending folds at a variety of scales, and thrust faulting. The resulting axial-plane cleavage fabric is particularly apparent in skarnified limestone units where it overprints the bedding [26].

Two types of mineralization are observed at Lened: emerald–scheelite bearing quartz veins and scheelite skarn orebodies. The emerald mineralization is displayed as an array of quartz veins hosted in a ca. 20 m lens of pyroxene–garnet–amphibole skarn, developed in the Rabbitkettle Fm [26]. The veins contain beryl or emeralds of variable clarity with crystals up to 2.5 cm in length and 0.17 ct in weight [26,34]. Previous authors estimate that less than 5% of the beryl crystals observed at Lened are colored deeply enough to be classified as emeralds [26]. The emerald-bearing quartz veins contain minor amounts of scheelite (<1%) and dravite [26]. Tungsten mineralization, developed as scheelite, is dominantly hosted by skarns in the Rabbitkettle Fm, but is also present in the veins, cutting the Lened pluton [29], and in one 10 cm-wide pegmatite outcropping near the skarn [26]. While scheelite occurs in all skarn types (garnet–pyroxene, pyroxene, amphibole and biotite skarns), it is most abundant in the paragenetically late biotite skarn [28]. Detailed petrographic information on the skarn facies observed at Lened can be found in [28].

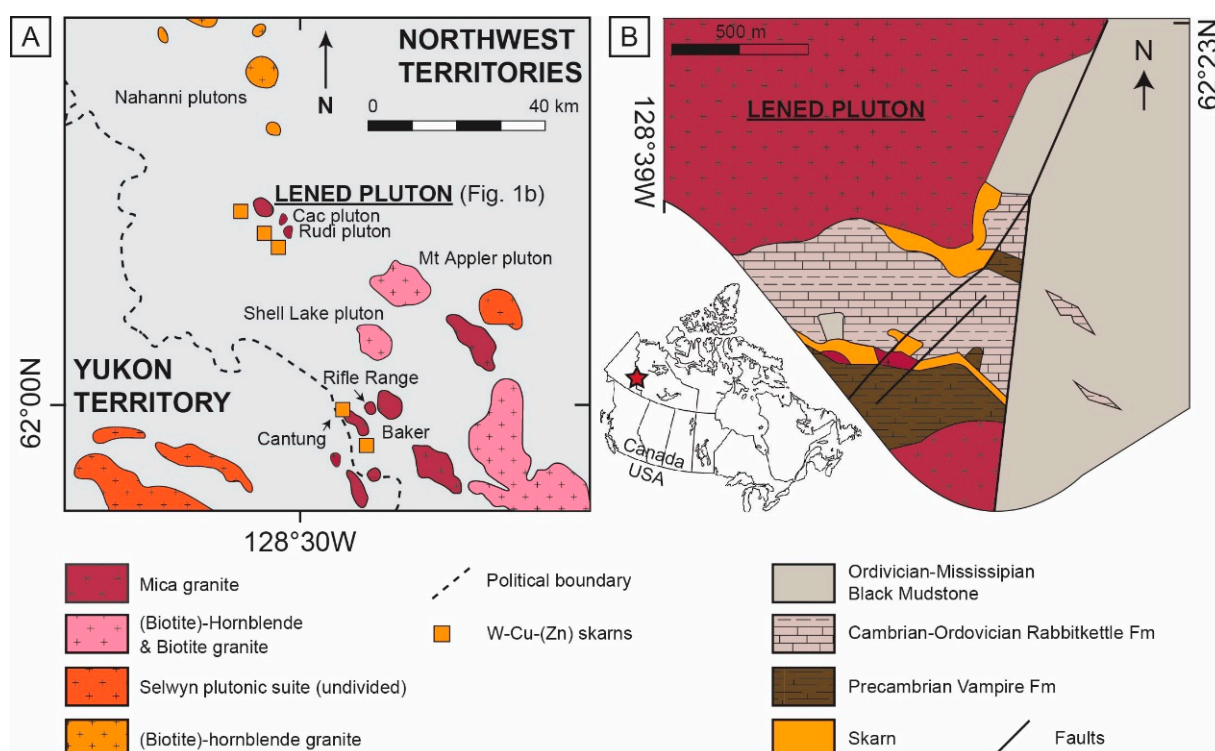


Figure 1. (A) Simplified regional map showing the location of granitic plutons and skarns within the Tungsten belt (modified after [35]), and (B) local map of the Lened W-(Be) deposit (modified after [26]), representing the whole sampling area for this study.

Two types of fluid inclusions, hosted in quartz and beryl from the emerald-bearing quartz veins, have been previously documented: aqueous-carbonic fluid inclusions associated with quartz and beryl, and later, brine inclusions associated with quartz only [32]. Neither of the two types could be identified as primary in origin by [32]. The aqueous-carbonic fluid inclusions within the beryl consist of approximately 4.5 mol.% CO₂ trapped between 200 and 610 °C at a maximum pressure of 320 MPa under lithostatic conditions [32]. The temperature of emerald vein formation is constrained at ca. 350 °C according to oxygen isotopic data acquired on quartz and biotite crystals [26]. The ore fluid is also inferred to have a significant amount of fluorine, which was incorporated into the vein and skarn minerals, such as micas and tourmaline [26].

The current model for the formation of the Lened deposit proposes a magmatic origin for the ore fluids [26,32]. This fluid has been interpreted as exsolving from a nearby pluton of the Selwyn Plutonic Suite during its late crystallization and cooling [26,32]. The fluids

likely traveled along the regional thrust faults (Figure 1B) to form the skarns and subsequent emerald-bearing veins [32]. Tungsten, Be and B have been proposed to have a magmatic origin, exsolved from the cooling Lened pluton to form the veins and skarn. Due to their common source and similar processes, the veins and the skarn are believed to be genetically related [26].

3. Analytical Methods

3.1. Samples

Fifty-three samples from drill core and outcropping rocks, including emerald-bearing quartz veins, were collected for this study south of the Lened pluton, at the contact between the Vampire, Earn and Rabbitkettle formations, where emerald-bearing veins cross-cut the pyroxene-garnet skarn. The locality for the samples is described by [32] and [26]. From this collection, twenty nine skarn samples were described in detail in [28], and twenty four samples of cm-sized euhedral quartz from emerald bearing veins (Figure 2A) were examined for this study. In the vein samples, five minerals were identified, including quartz, beryl, tourmaline, muscovite and calcite; quartz was the predominant phase. Beryl is generally growing in cavities with euhedral quartz (Figure 2B), and tourmaline is intergrown with anhedral quartz (Figure 2C). The beryl quartz samples often show some muscovite alteration in pods and crosscutting calcite crystals.

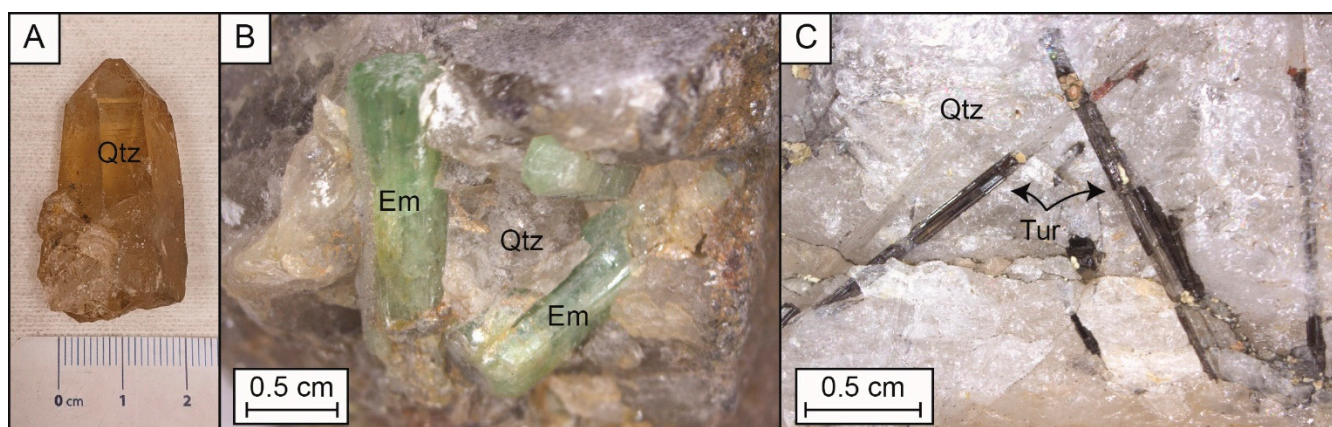


Figure 2. Photographs of the main minerals of interest of the Lened deposit. (A) Cm-sized euhedral quartz, (B) Intergrown euhedral quartz and emeralds, and (C) Intergrown anhedral quartz and euhedral tourmaline. Em: emerald (beryl), Qtz: quartz, Tur: tourmaline.

Emerald-beryl and tourmaline-bearing veins have been combined with previous paragenetic studies to define the relationship between B, W and Be in mineralizing fluids. However, samples for this study were limited and lacked good direct evidence of scheelite. Previous work at Lened indicated that scheelite mineralization occurred prior to, during and after quartz and beryl crystallization [26,28]. Additionally, scheelite and dravite inclusions have been reported in similar quartz-emerald veins; and emerald contains high W and B in its crystal structure [26]. Therefore, the fluids trapped in quartz are likely similar and related to the fluids that formed emerald, tourmaline and scheelite in the deposit, as suggested by previous authors [26].

3.2. Fluid Inclusion Petrographic and Microthermometric Investigations

Double-polished thick sections (200 μm) of euhedral quartz crystals associated with emerald-beryl mineralization were prepared for the fluid inclusion (FI) study. Petrographic observations were performed with a Zeiss Axioskop 40 optical microscope at the scale of the crystal to associate the fluid inclusion petrography with the crystallographic features of the minerals. Both sections and microscopic observations were performed at the University

of Alberta, Edmonton, AB, Canada. From the sections examined, one representative section was selected for this fluid inclusion study.

Any FIs with signs of stretching, necking-down or halos of small FIs that could reflect decrepitation or crystal-recovery processes were avoided [36]. Following the criteria of [37] and given the petrographic observations, no evidence for post-entrapment modification caused by diffusion or preferential H₂O loss was identified.

Microthermometric measurements of quartz-hosted fluid inclusions were performed with a Linkam THMSG600 heating-cooling stage mounted on an Olympus BX53M microscope at the University of Alberta (Edmonton, AB, Canada). The stage was calibrated with two synthetic standards by measuring the melting of solid CO₂ at −56.6 °C, the final melting of pure ice at 0.0 °C and pure water homogenization at 374 °C. Five phase transitions were recorded: melting of solid CO₂ (T_{m,car}), final melting of ice (T_{m,ice}), sassolite melting (T_{sas}), melting of clathrates (T_{m,cla}) and homogenization of CO₂ (T_{h,car}) temperatures. The temperatures of phase transitions are reported with an accuracy of approximately ±0.1 °C for melting temperatures and ±1 °C for homogenization temperatures. Due to the high proportion of CO₂ in the inclusions, total homogenization could not be measured due to decrepitation. All measurements can be found in Table S1, and a video is available as Video S2.

3.3. Raman Spectroscopy

Raman spectroscopic analyses of the gas, liquid phases and daughter minerals of the fluid inclusions were performed at GeoRessources laboratory (Nancy, France). Raman spectra were recorded with a LabRAM HR spectrometer (Horiba Jobin Yvon) equipped with a 600 gr.mm^{−1} grating and an edge filter. The confocal hole aperture was 1000 μm, and the slit aperture was 200 μm. The excitation beam was provided by a Stabilite 2017 Ar⁺ laser (Spectra Physics, Newport Corporation) at 514.53 nm and a power of 200 mW, focused on the sample using a 100× objective (Olympus). Acquisition time and number of accumulation were chosen to optimize the signal-to-noise ratio (S/N), ideally lower than 1%. Data were processed with LabSpec software [38], as defined by [39], and daughter minerals were identified with the CrystalSleuth software [40].

3.4. Laser Ablation Inductively Coupled Plasma Mass Spectrometry (LA-ICP-MS)

Selected major, minor and trace elements were measured in FIs in the selected quartz section at ETH Zürich (Zürich, Switzerland) with the ETH-prototype GeoLas system equipped with a 193-nm ArF-Excimer Compex 102F laser ablation system (LambaPhysik-Coherent) coupled to a Nexion2000 (PerkinElmer) fast-scanning quadrupole ICP mass spectrometer for multi-element analysis. The detailed specifications of this instrumentation are provided in [41]. LA-ICP-MS analyses were performed on the same FIs as those used for the microthermometry. Among the thirty FIs measured by microthermometry, twenty-five yielded LA-ICP-MS spectra that allowed processing. The sample was set within a small-volume (ca. 5 cm³), custom-made cylindrical glass ablation cell. Gas blanks and system contamination were minimized following the cleaning and setup procedures of [42]. The cell was fluxed with carrier gas consisting of high-purity (5.0 grade) He (1.1 L·min^{−1}). Sample gas consisting of 6.0 grade Ar (ca. 1 L·min^{−1}) was admixed downstream of the ablation cell prior to injection in the plasma. The ICP-MS was optimized for maximum sensitivity on the whole mass range and low oxide rate formation (²⁴⁸ThO⁺/²³²Th⁺ < 0.5%). The NIST-SRM610 glass [43] was used as an external standard for quantification of most trace elements, except for S, Cl and Br, which were calibrated against the Sca-17 scapolite standard [44]. Both were analyzed with a laser spot diameter of 40 μm, repetition rates of 10 Hz, fluence of ca. 5 J·cm^{−1} and a ca. 1 min measurement consisting of 30 s of a gas blank followed by 30 s ablation. For FIs, analyses were performed with a laser repetition rate of 15 Hz, fluence of ca. 14 to 18 J·cm^{−2} and variable spot sizes set so as to completely ablate the entire inclusion. FIs were analyzed by slowly incrementing the spot size with an opening aperture to prevent cracking [45]. The following isotopes were analyzed: ⁷Li, ⁹Be,

^{11}B , ^{23}Na , ^{24}Mg , ^{27}Al , ^{29}Si , ^{34}S , ^{35}Cl , ^{39}K , ^{42}Ca , ^{49}Ti , ^{55}Mn , ^{57}Fe , ^{63}Cu , ^{66}Zn , ^{75}As , ^{79}Br , ^{85}Rb , ^{88}Sr , ^{89}Y , ^{93}Nb , ^{95}Mo , ^{118}Sn , ^{121}Sb , ^{133}Cs , ^{138}Ba , ^{181}Ta , ^{182}W , ^{208}Pb and ^{209}Bi , with a dwell time of ca. 0.01 to 0.05 s per mass channel and a total sweep time of 3.75 to 7.5 s. These elements were selected according to previous publications in comparable W-mineralized systems (i.e., [10,17,46,47]). Data processing was performed with the Matlab[®]-based SILLS program [46]. Absolute element concentrations were calculated with the salinity measured by microthermometry as an internal calibration standard, after correction of the matrix signal using the stoichiometric concentrations of Si for quartz. Each ablation spectrum was carefully inspected during processing; spectra were only selected for element quantification if the ablation of the FI was controlled (i.e., not breached at the onset of ablation) and when the FI peak was distinguishable from the surface contamination peak [47]. Spectra showing contamination by solid inclusions in the matrix or by crystals accidentally trapped in the FIs were discarded. Analyte intensities in the matrix signal were generally constant and showed no evidence for significant zoning. Limits of detection (LODs) were calculated according to the method of [47]. All LA-ICPMS data are provided in Table S3.

4. Results

4.1. Fluid Inclusion Description and Raman Identification

From among the twenty-four quartz samples examined for this study, two were chosen for the fluid inclusion work. The quartz crystals were 5 cm along the c-axis, 2 cm in diameter and of euhedral shape (Figure 2A). The crystals were extracted from a vein sample where the cavities allowed the open space crystallization. In the selected sample, the emerald-beryl grew on the surface of the quartz, along the c-axis (Document S4). The filling of the vein was heterogeneous and did not include every mineral of interest in a single quality sample. The best examples of the relationship between quartz, tourmaline and emerald-beryl crystals are shown in Document S4. A detailed petrographic description of the vein was provided in [26].

A single and unique population of primary fluid inclusions was identified in all samples (Figure 3) with the same characteristics as the carbonic fluid population described in [32]. Fluid inclusions are either arranged in assemblage trails along, or isolated within, the growth zones of the crystals (Figure 3). This population of fluid inclusions was the only population encountered in our samples, and is therefore considered as one single fluid trapped during crystal growth. The length and shape of the individual fluid inclusions are variable, from 10 to 150 μm , elongated, irregular or negative-crystal shaped. This variation is randomly distributed across the crystal zones (Figure 3).

All fluid inclusions contain three phases at room temperature, $\text{H}_2\text{O}(\text{L})\text{--CO}_2(\text{L})\text{--CO}_2(\text{V})$, which show similar relative proportions among FIs (ca. 50% $\text{H}_2\text{O}(\text{L})$, 35% $\text{CO}_2(\text{L})$, 10% $\text{CO}_2(\text{V})$ and 5% sassolite). Some transparent solids occur at room temperature but are difficult to identify in fluid inclusions smaller than 50 μm (the solids are mainly observed during the T_{sas} phase transition while heating for microthermometry measurement). For that reason, a video has been added as Video S2. The solids are sub-transparent polygonal crystals residing in the aqueous phase. Raman identification peaks at 507 and 874 cm^{-1} indicate that this solid phase is the mineral sassolite (H_3BO_3) ([48]; Figure 3). In the aqueous phase, CO_2 and HCO_3^- were also detected by the Raman spectroscopy [48]. The H_2O band is also visible and shows weak deformation of the OH stretching vibration band, indicating a low concentration of dissolved chloride ions in the aqueous phase [49]. The carbonic liquid is dominantly CO_2 , but there are lower concentrations of CH_4 , H_2S and N_2 . The carbonic gaseous phase consists of major CO_2 and minor CH_4 mixtures (Figure 3). The main components of the fluid system are therefore $\text{H}_2\text{O}\text{--CO}_2\text{--NaCl}_{\text{eq}}\text{--H}_3\text{BO}_3$.

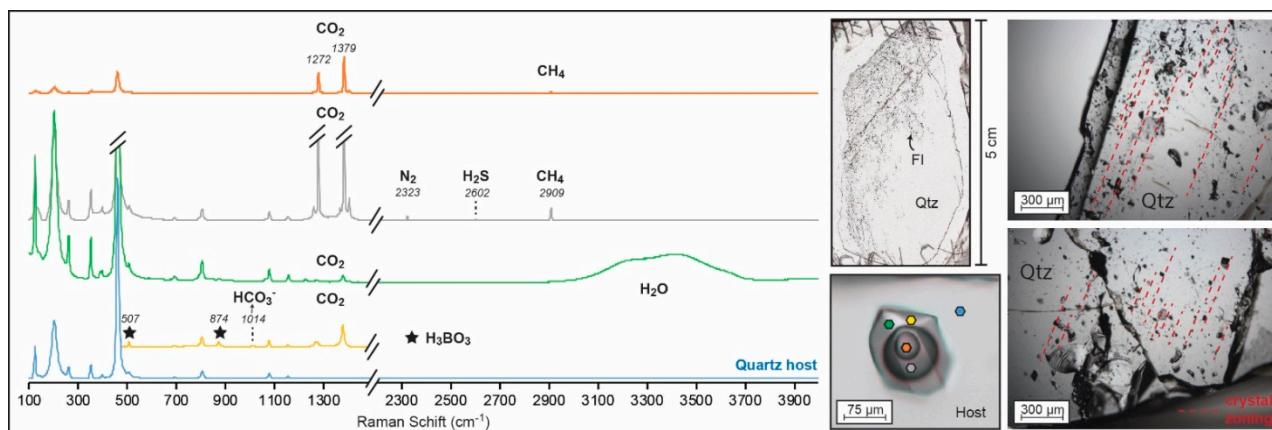


Figure 3. Representative Raman spectra of the multiple phases within the quartz-hosted Lened fluid inclusions compared to its host. For the green and yellow spectra, CO₂ is dissolved in the hydrous phase. The identification of species was performed following [48]. Orange and grey spectra correspond to gaseous and liquid CO₂, respectively; the green spectra shows the aqueous phase; and the yellow spectra is zoomed on the sassolite crystal peaks, which are highlighted by black stars. All peaks are compared to the quartz host spectra in blue. FI: fluid inclusion; Qtz: quartz. Pictures of the fluid inclusions along the crystal growth zoning are shown as references of the primary origin of the inclusions.

4.2. Microthermometric Measurements and Boron Concentration Calculations

Thirty primary fluid inclusions were measured by microthermometry and show similar results. All fluid inclusions measured by microthermometry have phase transition temperatures: $T_{m_{car}} = -57.3$ to -56.9 °C, $T_{m_{ice}} = -3.6$ to -2.6 °C, $T_{m_{cla}} = 8.8$ to 9.5 °C and $T_{h_{car}} = 21.3$ to 30.7 °C (refer to Section 3.2 for abbreviations). Sassolite crystals, when visible, melt between 8.9 and 10.7 °C (T_{sas}). Considering the homogeneity of the data acquired on single fluid inclusions, results are expressed to represent a comparable fluid, and the data are reported to reflect the characteristics of a homogeneous single fluid. With the exception of the sassolite melting temperatures not previously identified, this fluid inclusion population shares the same transition temperatures as the ones identified in quartz by [32] ($T_{m_{car}} = -59.1$ to -63.5 °C, $T_{m_{ice}} = -4.3$ to -2.3 °C, $T_{m_{cla}} = 8.6$ to 10.8 °C, and $T_{h_{car}} = 21.3$ to 28.7 °C).

Traditionally, salinity estimations by microthermometry, for FIs similar to those of our study, would be interpreted in the H₂O–NaCl or the H₂O–NaCl–CO₂ systems. However, high content in other components, such as boron, induces a systematic error in the fluid salinity calculation due to the complexity of this system and low salinity content [2]. In addition, routine trace element quantification strategies of LA-ICP-MS fluid inclusion signals are also performed on the basis of phase relations in chloride-dominated fluids [48,50,51] and hence do not consider H₃BO₃ as a potential major component. Therefore, NaCl_{eq} salinity as an internal standard for the reduction of the LA-ICP-MS data would result in systematically inaccurate results, and a different internal standard is required. In the system H₂O–NaCl_{eq}–H₃BO₃, B concentration is recommended as a more appropriate internal standard than NaCl_{eq} [2]. Currently, three techniques other than LA-ICP-MS allow quantifying B and salinity concentrations in fluid inclusions, two of which were used in the study for comparison (Figure 4).

The first technique uses the sassolite melting temperature (T_{sas}) measured by microthermometry [1]. With the $T_{m_{ice}}$ and T_{sas} temperatures, the amounts of NaCl_{eq} and H₃BO₃ can be estimated from solubility diagrams, which are available for several types of salts [1]. The fluid inclusions in this study contain dominantly NaCl, and to a lesser extent, KCl (see detailed concentrations in the following section). Therefore, the estimations were performed in the H₂O–NaCl–H₃BO₃ system, as shown in Figure 4A. Estimations in the

H₂O-NaCl-H₃BO₃ system from microthermometry measurements yielded 3.5 to 5 wt. % NaCl_{eq} and 3.0 to 3.5 wt. % H₃BO₃, respectively (Figure 4A).

The second method used the ratio of the Raman peak intensities corresponding to the H₃BO₃ and H₂O species [52]. In this study, the ratio of both peak intensities was ca. 0.04, which corresponds to a H₃BO₃ concentration of 3.5 ± 0.5 wt. % (Figure 4B).

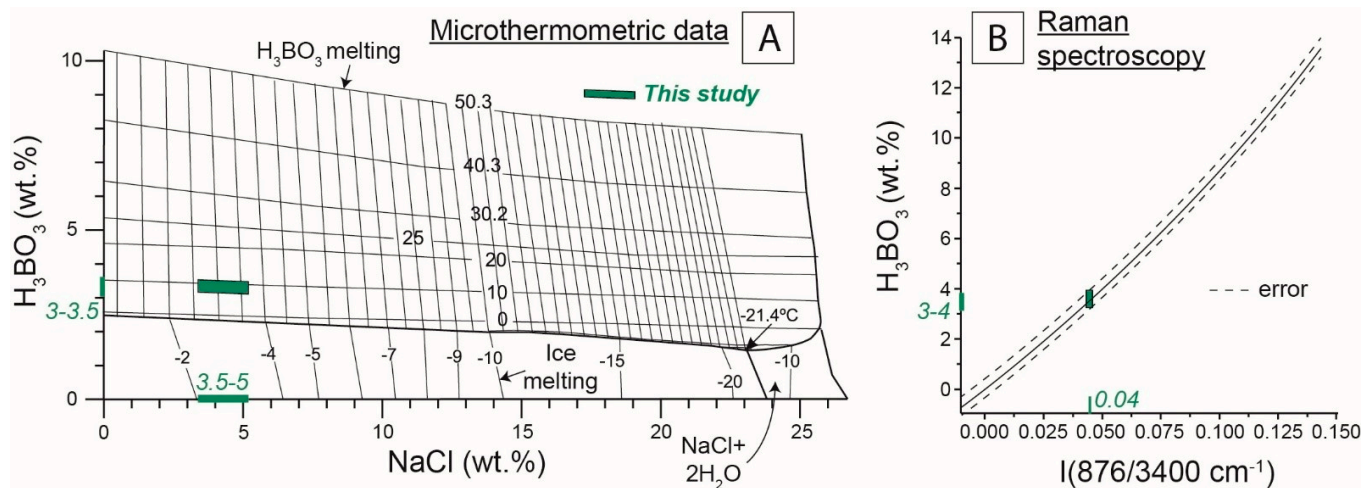


Figure 4. Boron and salinity concentration calculations. (A) Calculations from microthermometric results ($T_{m_{ice}}$ and T_{sas} dissolution temperatures; Table S1), from the solubility diagram of [1] in the H₂O-NaCl-H₃BO₃ system. (B) Calculation from the correlation between Raman spectroscopy intensity ratio of the boron and H₂O species bands and H₃BO₃ concentration according to [52].

A recent third method was proposed by [53] and considers the correlation between salinity, boron concentration and Raman spectroscopy peaks. The use of this method indicates a salinity lower than 5 wt. % NaCl, consistent with the microthermometry calculation method. However, the calculation of the H₃BO₃ concentrations with the method of [53] found the H₃BO₃ dissolved in the H₂O phase, as crystals of sassolite could not be identified. In this study, all the H₃BO₃ was forming H₃BO₃ crystal (sassolite), and we made our measurements from the peak of the sassolite crystal. Therefore, this method did not seem appropriate for our study.

Notably, our fluids also had a significant proportion of CO₂, which is not taken into account in these calculation methods. A supplementary CO₂ correction of the data is mentioned in the microthermometry calculation method but is not explicitly detailed in [1], and the influence of gaseous content on the Raman calculation is not mentioned in [50]. Since H₃BO₃ was not identified in the carbonic phases, the calculated value represents a maximum concentration for the whole fluid inclusion. However, the total salinity of the fluid remains uncertain. Salinity calculations using microthermometric data for the systems H₂O-NaCl and H₂O-CO₂-NaCl resulted in salinity of 4.5 to 6 wt. % NaCl_{eq} and 1.0 to 2.5 wt. % NaCl_{eq}, respectively [50,51], in comparison to the 3.5 to 5 wt. % NaCl_{eq} obtained in the H₂O-NaCl-H₃BO₃ system.

4.3. Trace Element Concentrations and Correlation

The maximum concentrations of major salt-forming ions normalized to 0.5 wt. % B were as follows (median of all analyses, $n = 25$): 1.8 wt. % Na, 0.2 wt. % K and 0.7 wt. % Cl, whereby NaCl is identified as the major salt. LA-ICP-MS data represents a single fluid inclusion from the quartz crystal shown in Figure 3.

In the analyses by LA-ICP-MS, sixteen elements were systematically above the limit of detection (see detailed results in Table S3). The three elements with the highest concentrations were the salt-forming elements: Na, K and Cl. When using 0.5 wt. % B as an internal standard, the fluid inclusions had relatively high concentrations of Li (40 to 474 ppm), Al (56 to 1003 ppm), As (36 to 490 ppm) and Cs (68 to 296 ppm); and lower concentrations

(i.e., generally less than a hundred ppm) of Rb (3.6 to 77 ppm), Sr (0.4 to 23 ppm), Sb (1 to 32 ppm), Ba (0.6 to 163 ppm), Mg (6.9 to 7.6 ppm) and elements of economic interest, such as Be (2.4 to 10.2 ppm), W (2.4 to 27 ppm) and Cu (5.1 to 73 ppm) (Figure 5). Due to the uncertainty associated with the boron abundance calculation from microthermometric and Raman spectroscopic measurements, we note that the uncertainty of the trace element concentrations is larger than the typical reproducibility (15–30% relative) reported by [54] (see Table S3). The concentrations are therefore interpreted to be semi-quantitative.

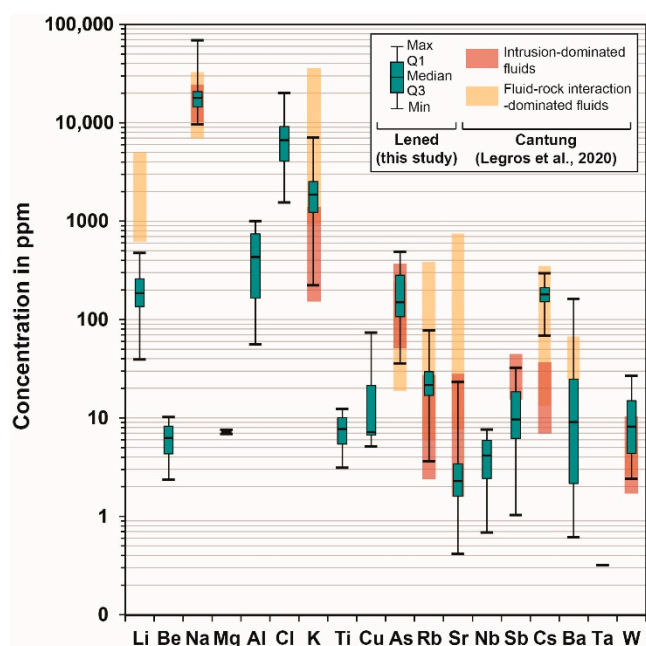


Figure 5. Trace element results for fluid inclusions (N = 25) of the Lened deposit (quartz host). All data are displayed as box and whisker plots showing the distribution of concentrations for each element, as minimum value (Min), first quartile (Q1), median, third quartile (Q3) and maximum value (Max). Individual analyses are not reported on the diagram, since all measurements are interpreted to belong to a single population. See detailed LA-ICPMS results within Table S3. The Lened data are compared to the Cantung W skarn deposit (located ca. 60 km SE of Lened, in the NWT, Canada; Figure 1A). The red boxes represent trace element data in fluid inclusions from intrusion-related fluids, and the yellow boxes represent trace element content of a more evolved fluid that interacted with the surrounding rocks [24] (both boxes represent minimum to maximum values).

5. Discussion

5.1. Salinity Calculation in a Boron-Rich System

Fluids associated with both Be and W mineralization in a system typically show low to medium salinity (<15 wt. % NaCl_{eq}), dominated by sodium-rich salts with homogenization temperatures below 400 °C [5,10,17,18,47,55]. While most fluids from these deposits are aqueous, the presence of other volatiles is common (CO_2 , CH_4 , N_2), and CO_2 is generally the predominant volatile species [56].

In this study, we were able to quantify for the first time the extent of uncertainty in salinity calculations in a typical aqueous low to medium salinity fluid system with significant concentrations of boron (Figure 6; Table S5). Calculations using the H_2O - NaCl_{eq} system overestimate the salinity for a B-rich system, where the highest bias occurs at low salinity (Figure 6A) with up to 70% error for salinity below 2 wt. % NaCl_{eq} and a boron concentration of 1.0 wt. % (Figure 6B). Therefore, considering boron for salinity calculations is very important in low-salinity systems, such as in tungsten ore systems, where B is usually present in the fluids [3] in concentrations from 0.1 to 1 wt. %, as reported by previous studies [10,17,18,57,58].

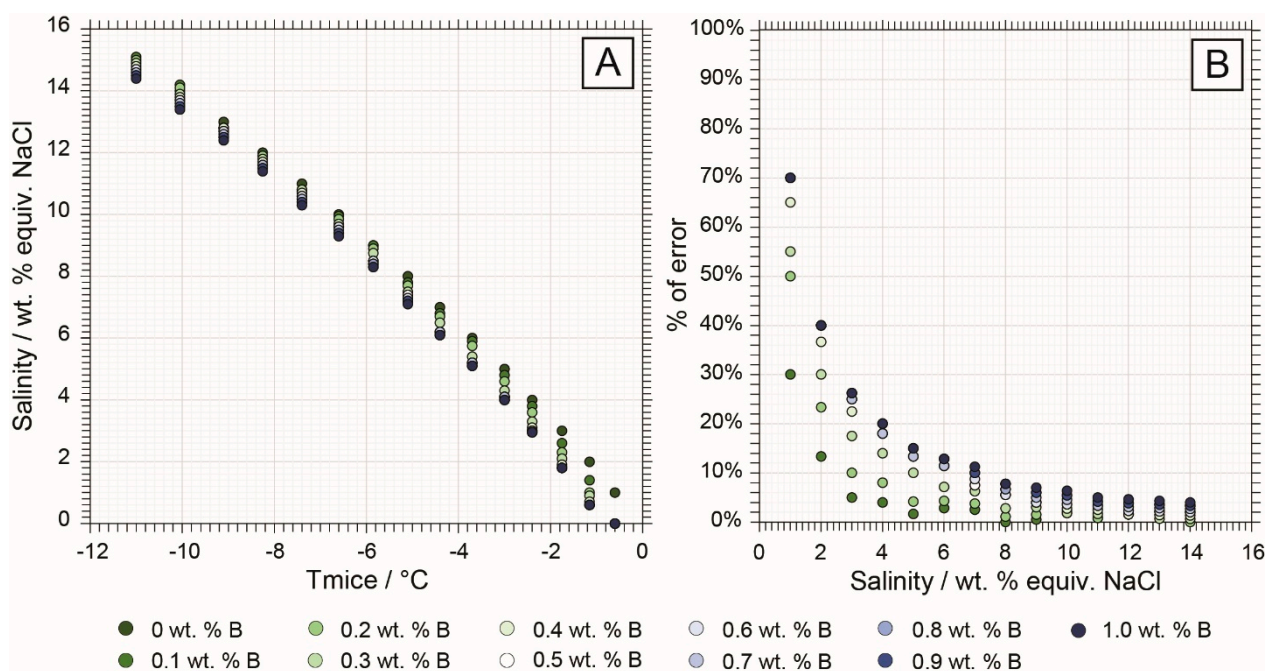


Figure 6. Salinity bias calculations comparing a H₂O-NaCl system and increment of 0.1 wt. % of boron. The comparison is made between salinity calculations in the H₂O-NaCl and H₂O-NaCl-H₃BO₃ for a range of salinity from 1 to 15 wt. % NaCl and boron concentrations between 0.1 and 1 wt. % (0.5 to 6 wt. % H₃BO₃) with microthermometry measurements only [1,50]. Detailed calculations are available in Table S5. (A) Case of a H₂O-NaCl-H₃BO₃ system where T_{sas} cannot be measured. Comparison of calculations bias at various salinity concentrations with increasing boron content using T_m_{ice} measurement only. (B) Error % made in the salinity calculation in a boron-rich system if boron concentration is not considered (calculation in the H₂O-NaCl system).

In low-salinity boron-dominated systems, changes in T_m_{ice} may reflect variations in salinity or in boron concentration due to this calculation bias. Chlorine, unlike boron, is incompatible in most minerals [59]. Therefore, in most magmatic-hydrothermal systems, changes in T_m_{ice} associated with chlorinity are commonly interpreted to represent fluid–fluid processes, such as fluid mixing or boiling. In contrast, B is readily incorporated as a major element into tourmaline and as a trace element in mica and feldspar. Therefore, changes in T_m_{ice} associated with varying B concentrations can also result from fluid–rock interaction or B fractionation out of the fluid and do not necessarily imply fluid–fluid processes.

No method for calculating salinity in the H₂O-CO₂-NaCl-H₃BO₃ system is currently described in the literature; therefore, we cannot assess the role of CO₂. In this study, the H₃BO₃ content calculated using the thermometric and the Raman methods yielded similar results. Therefore, the concentrations obtained are considered to provide a maximum B concentration for the fluid, and therefore, maximum trace element contents.

5.2. Magmatic Origin and Fluid-Rock Interaction

The Cs content (70–300 ppm) in fluid inclusions from Lened (Figure 5) is similar to that of other non-boiling fluids from rare metal magmatic-hydrothermal systems (<1000 ppm, commonly at ca. 100 ppm) [47,57,58,60]. Cesium behaves incompatibly during fractional crystallization of felsic magmas and becomes enriched in late-stage magmas and aqueous fluids [4,47,58]. Therefore, the fluid observed in the veins containing both scheelite and emerald-beryl at Lened likely reflects a fluid exsolved from a highly differentiated intrusion (likely the Lened pluton), as proposed by previous authors on the basis of stable isotope analysis and isochore calculations [26,32]. The Cs content in the Lened fluid inclusions is comparable to that of fluid inclusions in scheelite crystals from the Cantung skarn

deposit (45–380 ppm), located ca. 60 km southward [24]. From the literature on magmatic-hydrothermal ore systems (such as vein-type, porphyry, epithermal and Carlin W, Sn, Cu, Au, Mo, Pb, Zn rich-systems), high concentrations in B, Rb, K, As, Li and Sb and Cs in the fluid are commonly attributed to an origin through exsolution from a magma of intermediate to felsic composition [24,55,57,58,61–63]. In the case of Lened, the oxygen isotopic composition obtained from emerald samples by previous studies was consistent with fluids originating from the nearby plutons of the Selwyn Plutonic suite (Figure 1A) [32]. Our study is in agreement with current models of W, Cu and Be deposits showing that these elements (B, Rb, K, As, Li, Sb, Cs) originate from a magmatic fluid [5,55,57,58,61,62].

Divalent cations such as Ca, Sr and Ba are commonly identified in skarn-hosted fluids due to their interaction with carbonaceous metasedimentary host rocks [24,55]. At Lened, whole-rock analyses from the local limestone (Rabbitkettle Fm) shows expectedly high concentrations of Ca, Sr and Ba [26]. The fluid inclusion trace element data show the presence of Sr and Ba at low concentrations (Ca concentrations are below the limit of detection) (Figure 5) compared to fluid inclusions from the Cantung deposit [24]. Therefore, the amount of interaction of this fluid with the surrounding rocks is probably milder than described at Cantung, and of lesser importance for the ore deposition process.

The fluid observed at Lened likely represents: (i) a magmatic fluid exsolved from the intrusion prior to ore deposition (explaining the lack of scheelite crystals) and that started interacting with the metasedimentary rocks at Lened to leach the Ca, Sr and Ba later in the history of the deposit, or (ii) the fluid inclusions represent the ore fluid but already exhausted of Ca, Sr and Ba due to the precipitation of scheelite in nearby veins. Calcium is necessary for the crystallization of the main tungsten mineral, scheelite, which is also commonly enriched in Sr [50]. The first hypothesis seems the most probable in our case because we have no direct evidence of scheelite in the specific portion of the vein that we sampled (heterogeneous filling).

The Be mineralization at Lened is also characterized by an enrichment in vanadium in the emeralds crystals [32]. The emeralds are interpreted to originate from the interaction of a magmatic fluid with the host rocks, similarly to what described for the W mineralization, but in that case the local mudstone hosted the significant amount of V [26]. While we do not have any clear evidence of interaction with the local mudstone in this study, we assume that the metal-rich magmatic fluid, during its ascent, encountered multiple rock formations, which may include the V-rich mudstones, before interacting with the limestone and forming the scheelite-rich skarn, similarly to process recently described at the Dayakou emerald deposit in Southwest China [64].

The lack of boron in the remainder of the tungsten skarn [28] seems to suggest that these veins are independent of the fluids that formed the skarn, accompanying the majority of the tungsten deposit. Instead, these fluids appear to have followed the thrust fault and interacted with the V-rich mudstones to a greater degree than those that formed the skarn.

5.3. Fluid–Rock Interaction and Correlation to Fluid pH

The Lened fluid inclusions show the interaction of a magmatic fluid with the surrounding rocks. This agrees with the recent new classification of the Lened deposit in the emerald deposit group called: IB, magmatic-related interacting with sedimentary rocks [5]. While fluid–rock interaction is a common process involved in both emerald and tungsten deposits [5,10,28], the understanding of this interaction can be improved by the evidence of the boron-rich sassolite crystals.

The occurrence of sassolite within the fluid gives not only a direct indication of the high boron content of the fluid, but also of its pH. Boron occurs dominantly as H_3BO_3 species at pH between 1 and 4 [1,65]. The main tungsten species present in solution at pH < 4 is H_2WO_4 , transforming into HWO_4^- at higher and more neutral pH [66,67]. An increase in fluid pH induced by processes such as the CO_2 -degassing (common gas in both Be and W systems) and/or fluid–rock interactions (previously described models for tungsten precipitation [10,17]), will destabilize these polymeric tungstates to form WO_4^{2-} and

other monomeric tungstate [68], which can interact with metal cations to form wolframite ((Fe,Mn)WO₄) or scheelite (CaWO₄) [69]. This process is also relevant to the emerald-beryl deposit, where Be²⁺ has strong complexation as monomeric hydroxide complexes, such as BeOH⁺, Be(OH)_{2(aq)} and Be(OH)₃⁻ [70]. This is consistent with previous work suggesting that Be was transported in a low pH fluid and its complexation was destabilized by its interaction with the local limestone to precipitate the emeralds [26].

6. Conclusions

The Lened W-(Be) deposit features rare H₃BO₃-rich fluid inclusions that allow correlation of boron-rich magmatic fluid and metal enrichment in magmatic-hydrothermal skarn-vein systems. While the metals and boron are sourced from the magmatic intrusion, likely to be the Lened pluton, the boron concentration is not directly correlated to higher metal content in the fluid. The presence of sassolite (H₃BO₃) and the trace element concentrations indicate that the fluid observed at Lened is a magmatic and acidic fluid that slightly interacted with the surrounding metasedimentary rocks (evidenced by Sr and Ba). Its interaction with the local country rocks, and therefore, neutralization, is likely to be the trigger for the ore mineral precipitation.

Supplementary Materials: The following supporting information can be downloaded at: <https://doi.org/10.5281/zenodo.6603922>. Table S1: Detailed microthermometry measurements. Video S2: Microthermometry visualization of the typical phase transitions. Table S3: Detailed LA-ICPMS data. Document S4: Elements of petrography. Table S5: Detailed calculation of the error induced in salinity calculations for boron-enriched fluids.

Author Contributions: Investigation, H.L., V.E., O.L. and C.C.-M.; resources, writing—review and editing, H.L., V.E., O.L., P.L.-S., H.F., E.A. and C.C.-M.; supervision, P.L.-S.; funding acquisition, P.L.-S. and H.F. All authors have read and agreed to the published version of the manuscript.

Funding: This research was supported by the NSERC Discovery Grant to Pilar Lecumberri-Sanchez and the Polar Continental Shelf Project, and Northwest Territories Geological Survey contribution agreements.

Data Availability Statement: Not applicable.

Acknowledgments: We would like to thank the Northwest Territories Geological Survey for helping with access to the Lened site. We are also grateful to Marie-Camille Caumon (Georessources lab, Nancy) for her help with the Raman data acquisition.

Conflicts of Interest: The authors declare no conflict of interest.

References

1. Peretyazhko, I.S.; Prokof'ev, V.Y.; Zagorskii, V.E.; Smirnov, S.Z. Role of Boric Acids in the Formation of Pegmatite and Hydrothermal Minerals: Petrologic Consequences of Sassolite (H₃BO₃) Discovery in Fluid Inclusions. *Petrol. C/C Petrol.* **2000**, *8*, 214–237.
2. Sirbescu, M.-L.C.; Krukowski, E.G.; Schmidt, C.; Thomas, R.; Samson, I.M.; Bodnar, R.J. Analysis of Boron in Fluid Inclusions by Microthermometry, Laser Ablation ICP-MS, and Raman Spectroscopy: Application to the Cryo-Genie Pegmatite, San Diego County, California, USA. *Chem. Geol.* **2013**, *342*, 138–150. [[CrossRef](#)]
3. Slack, J.F.; Trumbull, R.B. Tourmaline as a Recorder of Ore-Forming Processes. *Elements* **2011**, *7*, 321–326. [[CrossRef](#)]
4. Hulsbosch, N.; Boiron, M.-C.C.; Dewaele, S.; Muchez, P. Fluid Fractionation of Tungsten during Granite–Pegmatite Differentiation and the Metal Source of Peribatholithic W Quartz Veins: Evidence from the Karagwe-Ankole Belt (Rwanda). *Geochim. Cosmochim. Acta* **2016**, *175*, 299–318. [[CrossRef](#)]
5. Giuliani, G.; Groat, L.A.; Marshall, D.; Fallick, A.E.; Branquet, Y. Emerald Deposits: A Review and Enhanced Classification. *Minerals* **2019**, *9*, 105. [[CrossRef](#)]
6. Meinert, L.D.; Dipple, G.M.; Nicolescu, S. World Skarn Deposits. In *One Hundredth Anniversary Volume*; Society of Economic Geologists: Littleton, CO, USA, 2005. [[CrossRef](#)]
7. Kelly, W.C.; Rye, R.O. Geologic, Fluid Inclusion, and Stable Isotope Studies of the Tin-Tungsten Deposits of Panasqueira, Portugal. *Econ. Geol.* **1979**, *74*, 1721–1822. [[CrossRef](#)]
8. Zhao, W.W.; Zhou, M.-F.; Li, Y.H.M.; Zhao, Z.; Gao, J.-F. Genetic Types, Mineralization Styles, and Geodynamic Settings of Mesozoic Tungsten Deposits in South China. *J. Asian Earth Sci.* **2017**, *137*, 109–140. [[CrossRef](#)]

9. LeBoutillier, N.G.; Camm, G.S.; Shail, R.K.; Bromley, A.V.; Jewson, C.; Hoppe, N. Tourmaline-Quartz-Cassiterite Mineralization of the Land's End Granite at Nanjizal, West Cornwall. *Geosci. South-West Engl.* **2002**, *10*, 312–318.
10. Lecumberri-Sanchez, P.; Vieira, R.; Heinrich, C.A.; Pinto, F.; Wälle, M. Fluid-Rock Interaction Is Decisive for the Formation of Tungsten Deposits. *Geology* **2017**, *45*, 579–582. [[CrossRef](#)]
11. Codeço, M.S.; Weis, P.; Trumbull, R.B.; Pinto, F.; Lecumberri-Sanchez, P.; Wilke, F.D.H. Chemical and Boron Isotopic Composition of Hydrothermal Tourmaline from the Panasqueira W-Sn-Cu Deposit, Portugal. *Chem. Geol.* **2017**, *468*, 1–16. [[CrossRef](#)]
12. Neiva, A.M.R.; Silva, M.; Gomes, M.E.P. Crystal Chemistry of Tourmaline from Variscan Granites, Associated Tin-Tungsten and Gold Deposits, and Associated Metamorphic and Metasomatic Rocks from Northern Portugal. *Neues Jahrb. für Mineral. J. Mineral. Geochemistry* **2007**, *184*, 45–76. [[CrossRef](#)]
13. Codeço, M.S.; Weis, P.; Trumbull, R.B.; Van Hinsberg, V.; Pinto, F.; Lecumberri-Sanchez, P.; Schleicher, A.M. The Imprint of Hydrothermal Fluids on Trace-Element Contents in White Mica and Tourmaline from the Panasqueira W-Sn-Cu Deposit, Portugal. *Miner. Depos.* **2020**, *56*, 481–508. [[CrossRef](#)]
14. Baksheev, I.A.; Trumbull, R.B.; Popov, M.P.; Erokhin, Y.V.; Kudryavtseva, O.E.; Yapaskurt, V.O.; Khiller, V.V.; Vovna, G.M.; Kiselev, V.I. Chemical and Boron Isotopic Composition of Tourmaline from the Mariinsky Emerald Deposit, Central Urals, Russia. *Miner. Depos.* **2018**, *53*, 565–583. [[CrossRef](#)]
15. Arif, M.; Henry, D.J.; Moon, C.J. Cr-Bearing Tourmaline Associated with Emerald Deposits from Swat, NW Pakistan: Genesis and Its Exploration Significance. *Am. Mineral.* **2010**, *95*, 799–809. [[CrossRef](#)]
16. Harlaux, M.; Kouzmanov, K.; Gialli, S.; Laurent, O.; Rielli, A.; Dini, A.; Chauvet, A.; Menzies, A.; Kalinaj, M.; Fontboté, L. Tourmaline as a Tracer of Late-Magmatic to Hydrothermal Fluid Evolution: The World-Class San Rafael Tin (-Copper) Deposit, Peru. *Econ. Geol.* **2020**, *115*, 1665–1697. [[CrossRef](#)]
17. Korges, M.; Weis, P.; Lüders, V.; Laurent, O. Depressurization and Boiling of a Single Magmatic Fluid as a Mechanism for Tin-Tungsten Deposit Formation. *Geology* **2018**, *46*, 75–78. [[CrossRef](#)]
18. Pan, J.-Y.; Ni, P.; Wang, R.-C. Comparison of Fluid Processes in Coexisting Wolframite and Quartz from a Giant Vein-Type Tungsten Deposit, South China: Insights from Detailed Petrography and LA-ICP-MS Analysis of Fluid Inclusions. *Am. Mineral. J. Earth Planet. Mater.* **2019**, *104*, 1092–1116. [[CrossRef](#)]
19. Peretyazhko, I.S.; Zagorsky, V.Y.; Smirnov, S.Z.; Mikhailov, M.Y.; Ye, V.; Smirnov, S.Z.; Mikhailov, M.Y. Conditions of Pocket Formation in the Oktyabrskaya Tourmaline-Rich Gem Pegmatite (the Malkhan Field, Central Transbaikalia, Russia). *Chem. Geol.* **2004**, *210*, 91–111. [[CrossRef](#)]
20. London, D. Internal Differentiation of Rare-Element Pegmatites: Effects of Boron, Phosphorus, and Fluorine. *Geochim. Cosmochim. Acta* **1987**, *51*, 403–420. [[CrossRef](#)]
21. Pollard, P.J.; Pichavant, M.; Charoy, B. Contrasting Evolution of Fluorine- and Boron-Rich Tin Systems. *Miner. Depos.* **1987**, *22*, 315–321. [[CrossRef](#)]
22. Pichavant, M.; Manning, D. Petrogenesis of Tourmaline Granites and Topaz Granites; the Contribution of Experimental Data. *Phys. Earth Planet. Inter.* **1984**, *35*, 31–50. [[CrossRef](#)]
23. Peretyazhko, I.S. Genesis of Mineralized Cavities (Miaroles) in Granitic Pegmatites and Granites. *Petrology* **2010**, *18*, 183–208. [[CrossRef](#)]
24. Legros, H.; Lecumberri-Sanchez, P.; Elongo, V.; Laurent, O.; Falck, H.; Adlakha, E.; Chelle-Michou, C. Fluid Evolution of the Cantung Tungsten Skarn, Northwest Territories, Canada: Differentiation and Fluid-Rock Interaction. *Ore Geol. Rev.* **2020**, *127C*, 103866. [[CrossRef](#)]
25. Michallik, R.M.; Wagner, T.; Fusswinkel, T. Late-Stage Fluid Exsolution and Fluid Phase Separation Processes in Granitic Pegmatites: Insights from Fluid Inclusion Studies of the Luumäki Gem Beryl Pegmatite (SE Finland). *Lithos* **2021**, *380*, 105852. [[CrossRef](#)]
26. Lake, D.J.; Groat, L.A.; Falck, H.; Mulja, T.; Cempírek, J.; Kontak, D.; Marshall, D.; Giuliani, G.; Fayek, M. Genesis of Emerald-Bearing Quartz Veins Associated with the Lened Wskarn Mineralization, Northwest Territories, Canada. *Can. Mineral.* **2017**, *55*, 561–593. [[CrossRef](#)]
27. Wilson, B.S. Colored Gemstones from Canada. *Rocks Miner.* **2009**, *85*, 24–43. [[CrossRef](#)]
28. Elongo, V.; Lecumberri-Sanchez, P.; Legros, H.; Falck, H.; Adlakha, E.; Roy-Garand, A. Paragenetic Constraints on the Cantung, Mactung and Lened Tungsten Skarn Deposits, Canada: Implications for Grade Distribution. *Ore Geol. Rev.* **2020**, *125*, 103677. [[CrossRef](#)]
29. Glover, J.K. Geology of the Lened Tungsten Skarn Deposit, Logan Mountains, Northwest Territories. *Miner. Depos. North. Cordillera. Canad. Inst. Min. Met.* **1986**, *37*, 255–265.
30. Rasmussen, K. The Timing, Composition, and Petrogenesis of Syn- to Post- Accretionary Magmatism in the Northern Cordilleran Miogeocline, Eastern Yukon and Southwestern Northwest Territories. Ph.D. Thesis, University of British Columbia, Vancouver, BC, Canada, 2013.
31. Government of Northwest Territories. A Guide to Mineral Deposits in the Northwest Territories. 2016. Available online: <https://www.iti.gov.nt.ca/sites/iti/files/mineraldeposites2-nocrops.pdf> (accessed on 31 March 2022).
32. Marshall, D.D.; Groat, L.A.; Falck, H.; Giuliani, G.; Neufeld, H. The Lened Emerald Prospect, Northwest Territories, Canada: Insights from Fluid Inclusions and Stable Isotopes, with Implications for Northern Cordilleran Emerald. *Can. Mineral.* **2004**, *42*, 1523–1539. [[CrossRef](#)]

33. Gordey, S.P.; Anderson, R.G. *Evolution of the Northern Cordilleran Miogeocline, Nahanni Map Area (105I), Yukon and Northwestern Territories*; Minister of Supply and Services Canada: Ottawa, ON, Canada, 1993; Volume Memoir 428, ISBN 066014963X.
34. Marshall, D.; Falck, H.; Mann, B.; Kirkham, G.; Mortensen, J. Geothermometry and Fluid Inclusion Studies of the E-Zone Biotite Skarn. *Cantung Mine Tungsten NWT* **2003**, *60*.
35. Rasmussen, K.L.; Mortensen, J.K. Magmatic Petrogenesis and the Evolution of (F: Cl: OH) Fluid Composition in Barren and Tungsten Skarn-Associated Plutons Using Apatite and Biotite Compositions: Case Studies from the Northern Canadian Cordillera. *Ore Geol. Rev.* **2013**, *50*, 118–142. [[CrossRef](#)]
36. Lambrecht, G.; Diamond, L.W. Morphological Ripening of Fluid Inclusions and Coupled Zone-Refining in Quartz Crystals Revealed by Cathodoluminescence Imaging: Implications for CL-Petrography, Fluid Inclusion Analysis and Trace-Element Geothermometry. *Geochim. Cosmochim. Acta* **2014**, *141*, 381–406. [[CrossRef](#)]
37. Bakker, R. Re-Equilibration Processes in Fluid Inclusion Assemblages. *Minerals* **2017**, *7*, 117. [[CrossRef](#)]
38. Schrötter, H.W.; Klöckner, H.W. Raman Scattering Cross Sections in Gases and Liquids. In *Raman Spectroscopy of Gases and Liquids*; Springer: Berlin/Heidelberg, Germany, 1979; pp. 123–166.
39. Burke, E.A.J. Raman Microspectrometry of Fluid Inclusions. *Lithos* **2001**, *55*, 139–158. [[CrossRef](#)]
40. Laetsch, T.; Downs, R.T. Software for identification and refinement of cell parameters from powder diffraction data of minerals using the RRUFF Project and American Mineralogist Crystal Structure Databases. In Proceedings of the 19th General Meeting of the International Mineralogical Association, Kobe, Japan, 23–28 July 2006; Volume 23, p. e28.
41. Laurent, O.; Guillong, M.; Heinrich, C.A.; Neubauer, K.; Stephan, C. Advantages of a Fast-Scanning Quadrupole for LA-ICP-MS Analysis of Fluid Inclusions. *J. Anal. At. Spectrom.* **2021**, *36*, 2043–2050. [[CrossRef](#)]
42. Schläglova, K.; Wälle, M.; Heinrich, C.A. LA-ICP-MS Analysis of Fluid Inclusions: Contamination Effects Challenging Micro-Analysis of Elements Close to Their Detection Limit. *J. Anal. At. Spectrom.* **2017**, *32*, 1052–1063. [[CrossRef](#)]
43. Jochum, K.P.; Weis, U.; Stoll, B.; Kuzmin, D.; Yang, Q.; Raczek, I.; Jacob, D.E.; Stracke, A.; Birbaum, K.; Frick, D.A. Determination of Reference Values for NIST SRM 610–617 Glasses Following ISO Guidelines. *Geostand. Geoanalytical Res.* **2011**, *35*, 397–429. [[CrossRef](#)]
44. Seo, J.H.; Guillong, M.; Aerts, M.; Zajacz, Z.; Heinrich, C.A. Microanalysis of S, Cl, and Br in Fluid Inclusions by LA-ICP-MS. *Chem. Geol.* **2011**, *284*, 35–44. [[CrossRef](#)]
45. Gagnon, J.E.; Samson, I.M.; Fryer, B.J.; Samson, I.M.; Anderson, A.J.; Marshall, D. LA-ICP-MS Analysis of Fluid Inclusions. Fluid Inclusions: Analysis and Interpretation. *Mineral. Assoc. Can. Short Course* **2003**, *32*, 291–318.
46. Guillong, M.; Meier, D.L.; Allan, M.M.; Heinrich, C.A.; Yardley, B.W.D. Appendix A6: SILLS: A MATLAB-Based Program for the Reduction of Laser Ablation ICP-MS Data of Homogeneous Materials and Inclusions. *Mineral. Assoc. Can. Short Course* **2008**, *40*, 328–333.
47. Pettke, T.; Oberli, F.; Audétat, A.; Guillong, M.; Simon, A.C.; Hanley, J.J.; Klemm, L.M. Recent Developments in Element Concentration and Isotope Ratio Analysis of Individual Fluid Inclusions by Laser Ablation Single and Multiple Collector ICP-MS. *Ore Geol. Rev.* **2012**, *44*, 10–38. [[CrossRef](#)]
48. Frezzotti, M.L.; Tecce, F.; Casagli, A. Raman Spectroscopy for Fluid Inclusion Analysis. *J. Geochem. Explor.* **2012**, *112*, 1–20. [[CrossRef](#)]
49. Caumon, M.-C.; Dubessy, J.; Robert, P.; Tarantola, A. Fused-Silica Capillary Capsules (FSCCs) as Reference Synthetic Aqueous Fluid Inclusions to Determine Chlorinity by Raman Spectroscopy. *Eur. J. Mineral.* **2013**, *25*, 755–763. [[CrossRef](#)]
50. Steele-MacInnis, M.; Lecumberri-Sanchez, P.; Bodnar, R.J. HokieFlincs_H2O-NaCl: A Microsoft Excel Spreadsheet for Interpreting Microthermometric Data from Fluid Inclusions Based on the PVTX Properties of H₂O-NaCl. *Comput. Geosci.* **2012**, *49*, 334–337. [[CrossRef](#)]
51. Steele-MacInnis, M. Fluid Inclusions in the System H₂O-NaCl-CO₂: An Algorithm to Determine Composition, Density and Isochore. *Chem. Geol.* **2018**, *498*, 31–44. [[CrossRef](#)]
52. Thomas, R. Determination of the H₃BO₃ Concentration in Fluid and Melt Inclusions in Granite Pegmatites by Laser Raman Microprobe Spectroscopy. *Am. Mineral.* **2002**, *87*, 56–68. [[CrossRef](#)]
53. Qiu, Y.; Zhang, R.; Chou, I.-M.; Wang, X.; Hu, W.; Zhang, W.; Lu, J.; Li, G.; Li, Z. Boron-Rich Ore-Forming Fluids in Hydrothermal W-Sn Deposits from South China: Insights from in Situ Raman Spectroscopic Characterization of Fluid Inclusions. *Ore Geol. Rev.* **2021**, 104048. [[CrossRef](#)]
54. Allan, M.M.; Yardley, B.W.D.; Forbes, L.J.; Shmulovich, K.I.; Banks, D.A.; Shepherd, T.J. Validation of LA-ICP-MS Fluid Inclusion Analysis with Synthetic Fluid Inclusions. *Am. Mineral.* **2005**, *90*, 1767–1775. [[CrossRef](#)]
55. Large, S.J.E.; Bakker, E.Y.N.; Weis, P.; Wälle, M.; Ressel, M.; Heinrich, C.A. Trace Elements in Fluid Inclusions of Sediment-Hosted Gold Deposits Indicate a Magmatic-Hydrothermal Origin of the Carlin Ore Trend. *Geology* **2016**, *44*, 1015–1018. [[CrossRef](#)]
56. Heinrich, C.A. The Chemistry of Hydrothermal Tin (-Tungsten) Ore Deposition. *Econ. Geol.* **1990**, *85*, 457–481. [[CrossRef](#)]
57. Audétat, A. The Metal Content of Magmatic-Hydrothermal Fluids and Its Relationship to Mineralization Potential. *Econ. Geol.* **2019**, *114*, 1033–1056. [[CrossRef](#)]
58. Legros, H.; Richard, A.; Tarantola, A.; Kouzmanov, K.; Mercadier, J.; Vennemann, T.; Maignac, C.; Cuney, M.; Wang, R.C.; Charles, N.; et al. Multiple Fluids Involved in Granite-Related W-Sn Deposits from the World-Class Jiangxi Province (China). *Chem. Geol.* **2019**, *508*, 92–115. [[CrossRef](#)]

59. Lecumberri-Sanchez, P.; Bodnar, R.J. Halogen Geochemistry of Ore Deposits: Contributions Towards Understanding Sources and Processes. In *The Role of Halogens in Terrestrial and Extraterrestrial Geochemical Processes*; Springer: Cham, Switzerland, 2018; pp. 261–305. [[CrossRef](#)]
60. Sciuba, M.; Beaudoin, G.; Grzela, D.; Makvandi, S. Trace Element Composition of Scheelite in Orogenic Gold Deposits. *Miner. Depos.* **2020**, *55*, 1149–1172. [[CrossRef](#)]
61. Heinrich, C.A.; Gunther, D.; Audétat, A.; Ulrich, T.; Frischknecht, R. Metal Fractionation between Magmatic Brine and Vapor, Determined by Microanalysis of Fluid Inclusions. *Geology* **1999**, *27*, 755–758. [[CrossRef](#)]
62. Landtwing, M.R.; Furrer, C.; Redmond, P.B.; Pettke, T.; Guillong, M.; Heinrich, C.A. The Bingham Canyon Porphyry Cu-Mo-Au Deposit. III. Zoned Copper-Gold Ore Deposition by Magmatic Vapor Expansion. *Econ. Geol.* **2010**, *105*, 91–118. [[CrossRef](#)]
63. Fiedrich, A.; Laurent, O.; Heinrich, C.A.; Bachmann, O. Melt and Fluid Evolution in an Upper-Crustal Magma Reservoir, Preserved by Inclusions in Juvenile Clasts from the Kos Plateau Tuff, Aegean Arc, Greece. *Geochim. Cosmochim. Acta* **2020**, *280*, 237–262. [[CrossRef](#)]
64. Long, Z.; Yu, X.; Zheng, Y. Ore Formation of the Dayakou Emerald Deposit (Southwest China) Constrained by Chemical and Boron Isotopic Composition of Tourmaline. *Ore Geol. Rev.* **2021**, *135*, 104208. [[CrossRef](#)]
65. Rasbury, E.T.; Hemming, N.G. Boron Isotopes: A “Paleo-PH Meter” for Tracking Ancient Atmospheric CO₂. *Elements* **2017**, *13*, 243–248. [[CrossRef](#)]
66. Wang, X.-S.; Timofeev, A.; Williams-Jones, A.E.; Shang, L.-B.; Bi, X.-W. An Experimental Study of the Solubility and Speciation of Tungsten in NaCl-Bearing Aqueous Solutions at 250, 300, and 350 °C. *Geochim. Cosmochim. Acta* **2019**, *265*, 313–329. [[CrossRef](#)]
67. Wood, S.A.; Samson, I.M. The Hydrothermal Geochemistry of Tungsten in Granitoid Environments: I. Relative Solubilities of Ferberite and Scheelite as a Function of T, P, PH, and m NaCl. *Econ. Geol.* **2000**, *95*, 143–182. [[CrossRef](#)]
68. Wang, X.; Qiu, Y.; Chou, I.; Zhang, R.; Li, G.; Zhong, R. Effects of PH and Salinity on the Hydrothermal Transport of Tungsten: Insights from In Situ Raman Spectroscopic Characterization of K₂WO₄-NaCl-HCl-CO₂ Solutions at Temperatures up to 400 °C. *Geofluids* **2020**, *2020*, 2978984. [[CrossRef](#)]
69. Wang, X.; Qiu, Y.; Lu, J.; Chou, I.-M.; Zhang, W.; Li, G.; Hu, W.; Li, Z.; Zhong, R. In Situ Raman Spectroscopic Investigation of the Hydrothermal Speciation of Tungsten: Implications for the Ore-Forming Process. *Chem. Geol.* **2020**, *532*, 119299. [[CrossRef](#)]
70. Wood, S.A. Experimental Determination of the Solubility of WO₃ (s) and the Thermodynamic Properties of H₂WO₄ (Aq) in the Range 300–600 C at 1 Kbar: Calculation of Scheelite Solubility. *Geochim. Cosmochim. Acta* **1992**, *56*, 1827–1836. [[CrossRef](#)]